J. Fluid Mech. (2012), *vol.* 708, *pp.* 329–348.
doi:10.1017/jfm.2012.313

Hydrodynamic wake resonance as an underlying principle of efficient unsteady propulsion

K. W. Moored[1]†, P. A. Dewey[1], A. J. Smits[1] and H. Haj-Hariri[2]

[1] Department of Mechanical and Aerospace Engineering, Princeton University, Princeton, NJ 08544, USA

[2] Department of Mechanical and Aerospace Engineering, University of Virginia, Charlottesville, VA 22904, USA

(Received 13 February 2012; revised 23 April 2012; accepted 18 June 2012; first published online 8 August 2012)

A linear spatial stability analysis is performed on the velocity profiles measured in the wake of an actively flexible robotic elliptical fin to find the frequency of maximum spatial growth, that is, the hydrodynamic resonant frequency of the time-averaged jet. It is found that: (i) optima in propulsive efficiency occur when the driving frequency of a flapping fin matches the resonant frequency of the jet profile; (ii) there can be multiple wake resonant frequencies and modes corresponding to multiple peaks in efficiency; and (iii) some wake structures transition from one pattern to another when the wake instability mode transitions. A theoretical framework, termed wake resonance theory, is developed and utilized to explain the mechanics and energetics of unsteady self-propulsion. Experimental data are used to validate the theory. The analysis, although one-dimensional, captures the performance exhibited by a three-dimensional propulsor, showing the robustness and broad applicability of the technique.

Key words: biological fluid dynamics, instability, swimming/flying, wakes/jets

1. Introduction

The phenomenon of unsteady propulsion has received considerable attention, especially in the context of swimming (Lauder & Drucker 2002) and flying (Lewin & Haj-Hariri 2003). Detailed studies of the force and moment production, and the structure of the wake have been reported, for two- and three-dimensional fins and aerofoils, using experiments and computations. What has been neglected, to some extent, is the connection between the dynamics of the fin, and the structure of the wake. In particular, we lack a full understanding of the conditions that lead to efficient propulsion, and how this condition makes itself evident in the flow field. Here, we examine the linear stability of the mean velocity profile in the wake of a undulating three-dimensional fin to show that the most unstable eigenmodes correspond directly to the wake structures observed in experiments, and that when the forcing frequency lies close to one of the resonant frequencies of the wake a peak is observed in the propulsive efficiency, η_p, where

$$\eta_p = \frac{\overline{T}U_\infty}{\overline{P}_{in}} \tag{1.1}$$

† Email address for correspondence: kmoored@princeton.edu

while U_∞ is the free-stream velocity, $\overline{T}$ is the time-averaged net thrust , and $\overline{P}_{in}$ is the time-averaged power input to the fluid.

The work of von Kármán & Burgers (1935) was the first to connect the forces and moments on a body to the momentum carried by the vortex system of the wake. In the context of unsteady propulsion, Triantafyllou, Triantafyllou & Grosenbaugh (1993) further investigated wake dynamics through a linear stability analysis of the time-averaged wakes behind a two-dimensional rigid pitching aerofoil (Koochesfahani 1987) as well as a two-dimensional heaving and pitching aerofoil. They only considered the development of the reverse von Kármán vortex street wake, where two single vortices are generated per flapping cycle (also called a 2S wake in the terminology of Williamson & Roshko 1988) and found that the propulsive efficiency was determined by the Strouhal number St, defined by

$$St = \frac{f A}{U_\infty} \tag{1.2}$$

where f is the linear frequency of motion, and A is the wake width. They found that a single peak in propulsive efficiency occurred in the range $0.25 \leqslant St \leqslant 0.35$ for their experimental data, and they proposed that this peak occurred at the frequency of maximum spatial growth of the instabilities of the velocity jet (Triantafyllou, Triantafyllou & Gopalkrishnan 1991; Triantafyllou *et al.* 1993), which in the present work is termed the hydrodynamic resonant frequency of the jet. At a fixed location downstream of the trailing edge of a flapping fin, they suggested that the perturbation waves will have the largest amplification (per unit input energy) at the resonant frequency of the jet profile (where there is maximum spatial growth), and that this will cause an expedient shear layer rollup and entrainment, and result in the strongest momentum jet for a given input energy. Thus a peak in the propulsive efficiency is expected when the fin is driven at the resonant frequency of the jet.

Although a survey of biological literature showed that many animals swim in the proposed optimal Strouhal number range (Triantafyllou *et al.* 1993), there are many cases where peak efficiency falls outside of this range (Anderson *et al.* 1998; Taylor, Nudds & Thomas 2003; Clark & Smits 2006; Buchholz & Smits 2008). Furthermore, elongated fish such as eels and lampreys typically generate 2P wake structures meaning that two pairs of vortices are shed per cycle (Hultmark, Leftwich & Smits 2007; Tytell *et al.* 2010). Fish with low-aspect-ratio propulsors such as rays can exhibit both 2S and 2P wake structures depending upon the fin kinematics (Dewey, Carriou & Smits 2011). Other more elaborate wake structures have also been observed in the wakes of heaving and pitching aerofoils (Lewin & Haj-Hariri 2003; Lentink *et al.* 2008).

For a two-dimensional heaving aerofoil, Lewin & Haj-Hariri (2003) utilized a linear stability analysis to show that multiple peaks in efficiency were related to cases where the driving frequency matched the resonant frequency of a jet where the jets implicitly depended on the amplitude of motion. They concluded that the Strouhal number alone was not sufficient to determine the conditions for efficiency, and what was needed was a combination of the Strouhal number and the reduced frequency ω, defined by

$$\omega = \frac{2\pi f L}{U_\infty} \tag{1.3}$$

where L is the chord length.

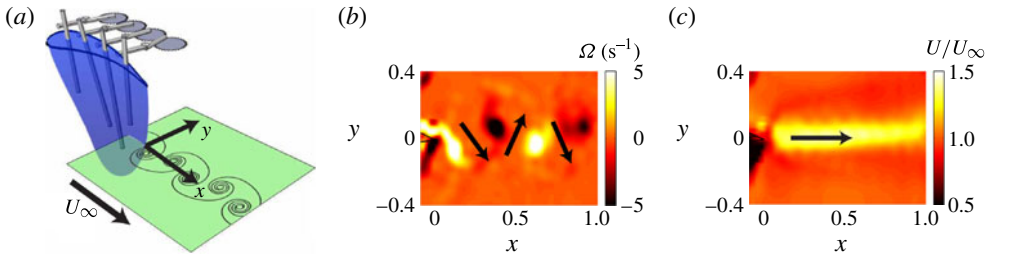

FIGURE 1. (Colour online) (*a*) Schematic of a ray-like robotic pectoral fin and the vortex wake structure in a laser-illuminated plane; (*b*) reverse von Kármán vortex street inducing a wavy jet; and (*c*) time-averaged velocity field. The x and y coordinates are non-dimensionalized with the chord length, L.

Here, we are interested in the performance of three-dimensional fins, in particular the swimming performance of actively flexible fins modelling the pectoral fins of rays studied by Clark & Smits (2006) and Dewey *et al.* (2011). In these experiments, the fin was actuated in a travelling wave motion that propagated from the leading edge to the trailing edge (see figure 1). Efficiency measurements were taken at two non-dimensional travelling wavelengths of $\lambda^* = \lambda/L = 6$ and 4, where λ is the wavelength. For both cases, multiple peaks in efficiency were seen as the Strouhal number was varied. Moreover, Dewey *et al.* (2011) found that at a fixed λ^* the wake structure transitioned from $2P$ to $2S$ with increasing Strouhal number. Although the analysis presented in this paper is used to examine the connection between the performance and the wake structure of bio-robotic ray-like fins, the theory is believed to be broadly applicable to other flapping foils.

To examine these flows further, we extend the work of Triantafyllou *et al.* (1993) and Lewin & Haj-Hariri (2003) to show that observed multiple peaks in efficiency, as well as the transitions in the wake patterns, can be explained by using a linear spatial stability analysis. This analysis provides a framework for assessing and achieving efficient unsteady self-propulsion, which we will call wake resonance theory.

The instantaneous flow field is characterized by the formation of wavy jet structures (figure 1*b*). In analogy with linear stability analysis applied to bluff bodies (Triantafyllou, Triantafyllou & Chryssostomidis 1986; Karniadakis & Triantafyllou 1989), we will analyse only the time-averaged flow field (figure 1*c*). In most cases, the jet can be considered weakly non-parallel, meaning that the characteristic length scale of a velocity profile changes slowly in the downstream direction compared to the instability wavelength (Chomaz 2005), and we will assume that such flows may be analysed using a local spatial stability analysis.

Using wake resonance theory, it will be shown that: (i) local optima in propulsive efficiency occur when the driving frequency of a flapping fin matches the hydrodynamic resonant frequency of the jet profile; (ii) there can be multiple wake resonant frequencies and modes corresponding to multiple peaks in efficiency; and (iii) some wake structures transition from one pattern to another when the wake instability mode transitions.

The analysis, although one-dimensional, captures all the major aspects of the performance exhibited by a three-dimensional propulsor, demonstrating the robustness and broad applicability of the technique.

2. The eigenvalue problem

The linear spatial stability analysis follows standard procedures. A one-dimensional (locally parallel) base flow is identified, $\boldsymbol{U} = [U(y), 0]$, and a small perturbation, $\boldsymbol{u} = [u, v]$, is superimposed onto the base flow and substituted into the Navier–Stokes and continuity equations. The equations are then linearized and a travelling wave form of the solution is assumed for the velocity perturbations, or equivalently, for the stream function perturbations. The result is the Orr–Sommerfeld equation for the complex amplitude, $\phi(y)$, of the wave-like perturbation to the stream function, $\psi(x, y, t)$, given by (with $\mathrm{D} \equiv \mathrm{d}/\mathrm{d}y$):

$$\{(\mathrm{D}^2 - \alpha^2)^2 - \mathrm{i}\, Re[(\alpha U - \omega)(\mathrm{D}^2 - \alpha^2) - \alpha U'']\}\phi = 0 \tag{2.1}$$

where

$$\psi(x, y, t) = \phi(y)\, \mathrm{e}^{\mathrm{i}(\alpha x - \omega t)} \equiv \phi(y)\ E, \tag{2.2}$$

$$u(x, y, t) = \frac{\partial \psi}{\partial y}, \tag{2.3}$$

$$v(x, y, t) = -\frac{\partial \psi}{\partial x}. \tag{2.4}$$

All parameters and variables are non-dimensionalized using the characteristic length and velocity scales L and U_∞, respectively. The complex wavenumber is $\alpha = \omega/c$ where c is the complex phase velocity.

In general both the wavenumber and frequency can be complex. However, a spatial stability analysis can be performed when the wavenumber is complex and the frequency is real, and a temporal stability analysis can be performed when the wavenumber is real and the frequency is complex. Since the time-averaged jets behind flapping foils are only weakly non-parallel and exhibit a convectively unstable region (Triantafyllou *et al.* 1993), we use a spatial stability analysis (Mattingly & Criminale 1972). Since the frequency is real, the temporal growth rate is zero (that is, the imaginary component $\omega_i = 0$), although the wavenumber is complex ($\alpha = \alpha_r + \mathrm{i}\alpha_i$). As can be seen from (2.2), if α_i is negative when $x > 0$ (downstream of the perturbations), the stream function and velocity perturbations will grow in space (spatial instability).

The boundary conditions that ensure decay of perturbations away from the centreline of a jet in an unbounded domain are the following:

$$\phi(\pm\infty) = 0, \tag{2.5}$$

$$\frac{\mathrm{d}\phi}{\mathrm{d}y}(\pm\infty) = 0. \tag{2.6}$$

The spatial stability problem forms a nonlinear eigenvalue problem with the complex eigenvalues α appearing up to and including the fourth power. The associated eigenmode is $\phi(y)$. To solve the eigenvalue problem a numerical solution is necessary (Orszag 1971).

3. Numerical solution

A general physical disturbance can be represented as a Fourier series that contains all of the frequency content in a flow (Gaster 1965; Huerre & Monkewitz 1985). Thus, one must solve for the eigenvalues over a range of real 'excited' frequencies, ω, to determine which mode and thus which frequency is the most unstable. For each velocity profile a range of ω is chosen and the eigenvalues are solved for each real

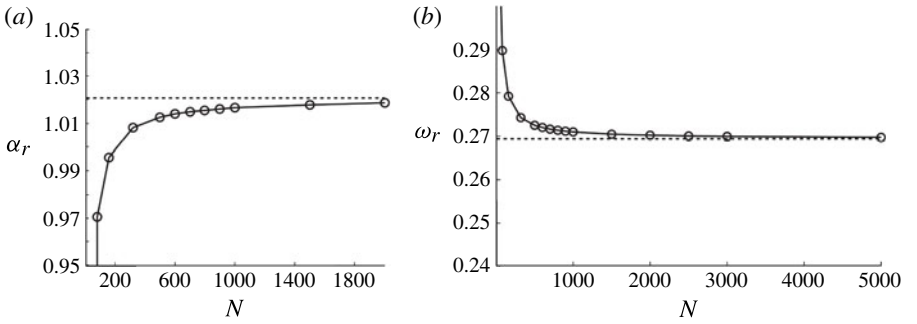

FIGURE 2. Accuracy test of the canonical case of plane Poiseuille flow with N discretization points. The dashed lines are the accurate values found by Orszag (1971). (*a*) The calculation of α_r using a spatial analysis with $\omega_r = 0.269$. (*b*) The calculation of ω_r using a temporal analysis with $\alpha_r = 1.021$.

frequency. To solve the nonlinear eigenvalue problem, the Orr–Sommerfeld equation is first expanded in powers of α,

$$\overbrace{(\phi)}^{C_0}\alpha^4 + \overbrace{(\mathrm{i}\,Re\,U\phi)}^{C_1}\alpha^3 + \overbrace{\left(-2\phi'' - \mathrm{i}\,Re\,\omega\phi\right)}^{C_2}\alpha^2 + \cdots \underbrace{\left(\mathrm{i}\,Re\,U''\phi - \mathrm{i}\,Re\,U\phi''\right)}_{C_3}\alpha + \underbrace{\left(\phi'''' + \mathrm{i}\,Re\,\omega\phi''\right)}_{C_4} = 0, \quad (3.1)$$

and then discretized over $y \in [-Y, Y]$, along with the boundary conditions (2.5) and (2.6), for some large value of Y.

The fourth-order nonlinear eigenvalue problem is linearized in α by casting it into the companion matrix form (Gantmacher 1959; Bridges & Morris 1984*a*; Haj-Hariri 1988)

$$\left\{\begin{bmatrix} -\boldsymbol{C}_0^{-1}\boldsymbol{C}_1 & -\boldsymbol{C}_0^{-1}\boldsymbol{C}_2 & -\boldsymbol{C}_0^{-1}\boldsymbol{C}_3 & -\boldsymbol{C}_0^{-1}\boldsymbol{C}_4 \\ \boldsymbol{I} & \boldsymbol{0} & \boldsymbol{0} & \boldsymbol{0} \\ \boldsymbol{0} & \boldsymbol{I} & \boldsymbol{0} & \boldsymbol{0} \\ \boldsymbol{0} & \boldsymbol{0} & \boldsymbol{I} & \boldsymbol{0} \end{bmatrix} - \alpha \begin{bmatrix} \boldsymbol{I} & \boldsymbol{0} & \boldsymbol{0} & \boldsymbol{0} \\ \boldsymbol{0} & \boldsymbol{I} & \boldsymbol{0} & \boldsymbol{0} \\ \boldsymbol{0} & \boldsymbol{0} & \boldsymbol{I} & \boldsymbol{0} \\ \boldsymbol{0} & \boldsymbol{0} & \boldsymbol{0} & \boldsymbol{I} \end{bmatrix}\right\} \boldsymbol{q} = \begin{bmatrix} \boldsymbol{0} \\ \boldsymbol{0} \\ \boldsymbol{0} \\ \boldsymbol{0} \end{bmatrix} \quad (3.2)$$

where

$$\boldsymbol{q} = [\alpha^3\boldsymbol{\phi}, \alpha^2\boldsymbol{\phi}, \alpha\boldsymbol{\phi}, \boldsymbol{\phi}]^{\mathrm{T}}, \quad (3.3)$$

and the matrices $\boldsymbol{C}_i$ are the discretized versions of the operators C_i in (3.1) with N discretization points.

The linear eigenvalue problem can be solved using standard techniques. The accuracy of the eigenvalue numerical solution was established by benchmarking against the eigenvalues of plane Poiseuille flow calculated by Orszag (1971), who found a critical Reynolds number for which the imaginary parts of the frequency and wavenumber are both zero and the real parts are $\omega_r = 0.269$ and $\alpha_r = 1.021$, respectively. Figure 2 shows the convergence of the current numerical solution to the previous solution for both the spatial formulation and the temporal formulation.

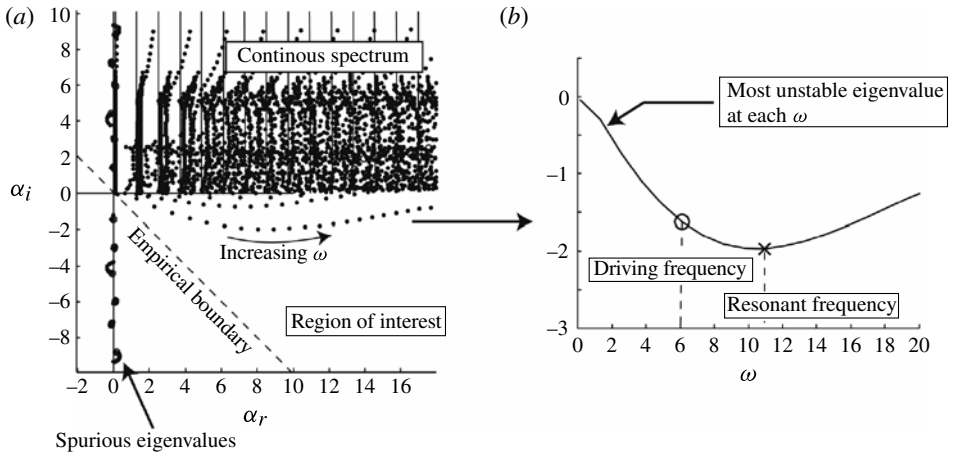

FIGURE 3. (*a*) Eigenvalues (·) in the complex-α plane at 40 different frequencies and (*b*) an extracted stability curve composed of the most unstable eigenvalues at each frequency. The solid lines in (*a*) are the exact continuous spectrum while the dashed line is the empirical boundary. Only the region of interest is searched for the most unstable eigenvalues. A resonant frequency of a velocity jet occurs at a local minimum in the stability curve. When the driving frequency matches the velocity-jet resonant frequency it is hypothesized that a local peak in propulsive efficiency occurs.

In the analysis of the experimental data, 200 discretization points were used for the computations. Doubling the discretization from 200 points to 400 points caused a change of less than 1 % in the real and imaginary parts of the eigenvalues.

The solution of the companion matrix is a globally convergent solution that does not need an initial guess. The numerical solution solves for the eigenvalue spectrum of the discretization which is a subset of the entire physical eigenvalue spectrum, augmented by spurious eigenvalues. The eigenmodes, $\boldsymbol{\phi}$, are recovered from $\boldsymbol{q}$.

The numerical eigenvalue problem admits $4N$ eigenvalues which can be plotted in a complex-α plane, as shown in figure 3(*a*). The physical eigenvalues fall into two categories: the discrete spectrum, and the continuous spectrum. The discrete spectrum corresponds to the proper eigenfunctions which are square integrable, and which satisfy $\phi'(y) \to 0$ as $|y| \to \infty$. In contrast, the continuous spectrum is composed of improper eigenfunctions which are not square integrable because their behaviour at large $|y|$ is oscillatory and only bounded, as opposed to decaying (Grosch & Salwen 1978; Salwen & Grosch 1981). Therefore, use of the relaxed boundary condition

$$\phi, \phi' \text{ bounded} \quad \text{as } y \to \pm\infty \tag{3.4}$$

leads to the simultaneous determination of a finite number of discrete eigenvalues with associated eigenfunctions and a set of continuous eigenvalues and eigenfunctions (Mack 1976). The numerical scheme utilizing the companion matrix recovers some of the oscillatory continuous modes (Bridges & Morris 1984*b*; Haj-Hariri 1988). Exact solutions for the four branches of the continuous spectrum have been found by Salwen & Grosch (1981) by determining the asymptotic behaviour ($y \to \infty$) of the Orr–Sommerfeld equation in an unbounded flow. Using a parameter k, the branches

are given by

$$\alpha_{1,2} = \pm\left(\frac{\omega}{\gamma}\right) - \mathrm{i}\,Re\left[\frac{1}{2}(1 \mp \gamma) \mp \frac{(\omega/Re)^2}{\gamma^3}\right] \quad \text{and} \quad \alpha_{3,4} = \pm \mathrm{i}\,k \tag{3.5}$$

where $\gamma = \sqrt{1 + 4k^2/Re^2}$ and $0 \leqslant k \leqslant \infty$.

The first and second branches of the continuous spectrum are found in the first and third quadrants of the complex-α plane while the third and fourth branches are found along the imaginary axis. As stated previously, the hypothesis is that driving a fin at the frequency of the most unstable eigenvalue of the time-averaged jet structure leads to a peak in efficiency. Thus the only solutions of interest are the ones with unstable eigenvalues. The right half of the complex-α plane corresponds to downstream-travelling waves where the waves are growing exponentially (unstable) if $\alpha_i < 0$. The left half of the complex-α plane corresponds to the upstream-travelling waves where the waves are growing exponentially (unstable) if $\alpha_i > 0$. In the case of the flapping fin, only downstream solutions are of interest. As such, only the fourth quadrant needs to be searched for eigenvalues. The continuous spectrum does not fall into the region of interest but, due to the numerical approximation, some spurious approximations of the continuous modes of the fourth branch do appear in the fourth quadrant (see spurious eigenvalues in figure 3). To eliminate these unphysical eigenvalues, a new search region is defined by the intersection of two regions:

$$(\alpha_r > -\alpha_i) \cap (\alpha_i < 0). \tag{3.6}$$

This relation is empirical in nature. All of the eigenvalues of the numerical scheme are examined in the complex-α plane to ensure that none of the physical eigenvalues leave the region of interest. In all of the cases presented in this paper, none of the physical unstable eigenvalues venture outside this region.

The eigenvalues are computed from a single velocity profile at 50 different frequencies with 200 discretization points admitting 40 000 eigenvalues. As can be seen in figure 3(*b*), the most unstable eigenvalue as a function of frequency has the largest spatial growth rate at a particular frequency, termed the 'resonant frequency' of that velocity profile. The eigenfunction that is the most unstable will change as a function of frequency. Once the empirical relation is checked, then the relevant information to extract from figure 3(*a*) is only the most unstable eigenvalue and eigenfunction at each frequency, forming the stability curve (figure 3*b*).

4. Resonant frequencies and modes

4.1. *Stability curves: efficiency condition*

A stability curve is generated for each velocity profile. The first important point on the stability curve is the driving frequency, which is the frequency at which the velocity profile was generated. The second important point is the resonant frequency, which is the frequency of maximal spatial amplification of the perturbation waves for that given profile.

It has been suggested (Triantafyllou *et al.* 1993) that when the driving frequency and the resonant frequency coincide then there is a local peak in the propulsive efficiency. This observation is confirmed in our work. When the driving frequency is coincident with the resonant frequency of a velocity profile we describe this unique frequency as a *wake resonant frequency*.

If, as in figure 3(*b*), the driving frequency of the fin is lower than the resonant frequency of the wake then increasing the driving frequency will bring the two

points closer together. However, each time the driving frequency is changed, the velocity profile is also changed and a new stability curve is generated. Thus the only truly physically realizable point on the stability curve is the eigenvalue at the driving frequency. Even though this is the case, an infinitesimal change in the driving frequency will, in most cases, cause an infinitesimal change in the velocity profile shape leading to the stability curve being only approximate in the neighbourhood of the driving frequency. This is particularly important as the slope of the stability curve at the driving frequency indicates whether the frequency needs to be tuned upward or downward to attain resonance. Although the direction of the actual resonant frequency is known, its location is unknown until the driving frequency matches the resonant frequency. Otherwise the location of the resonant frequency is only approximate. In particular, when the resonant frequency is far away from the driving frequency its actual location is not well known.

4.2. *Vorticity perturbations*

For each eigenvalue there is an associated eigenfunction, $\phi(y)$. As mentioned previously, the eigenfunctions relate to stream function perturbations and thus velocity perturbations that must be superimposed onto the base flow. The linear vorticity perturbation can also be obtained from $\phi(y)$ and captures many of the features of the observed wake structures.

The wake acts as a tuned amplifier for disturbances. In the case where there is no external forcing and the flow is convectively unstable, noise perturbations in the flow are amplified and convected downstream. The perturbations with the largest spatial growth rate (i.e. at a preferred frequency) will grow the fastest and dominate the observed wake structure. Note that the velocity perturbations have both a streamwise and cross-stream component.

In the case where there is external forcing (as in a flapping fin), a specific driving frequency is prescribed. Linear stability analysis will determine at which frequency there is a maximum amplification of the input perturbations, but the observed frequency, that is, the shedding frequency, will be that of the driving frequency of the fin. Thus we expect that the eigenvalue and eigenfunction at the driving frequency will relate to the observed wake structures. The total velocity field $\boldsymbol{u}_T$ is calculated as the superposition of the base flow and the perturbation velocity field, as in

$$\boldsymbol{u}_T(x, y, t) = \boldsymbol{U}(y) + \epsilon\, \boldsymbol{u}(x, y, t) \quad \text{with } \boldsymbol{u} = [u, v] \tag{4.1}$$

where $u = \mathrm{Re}\{\mathrm{D}\phi\ E\}$ and $v = \mathrm{Re}\{-\mathrm{i}\alpha\phi\ E\}$, $\mathrm{Re}\{\cdot\}$ denotes the real part of its argument, and E is defined in (2.2). The small constant ϵ is set throughout this paper in the range $1 \times 10^{-5} \leqslant \epsilon \leqslant 4 \times 10^{-5}$. The total vorticity field is given by

$$\Omega_T = -\frac{\partial \boldsymbol{U}}{\partial y} - \epsilon \mathrm{Re}\{(\mathrm{D}^2 - \alpha^2)\phi\ E\} \tag{4.2}$$

where the chosen value of ϵ produces a vorticity perturbation with the peak vorticity being small compared to the vorticity in the base flow.

5. Experimental setup

The data used for the stability analysis were obtained from the experiments by Dewey *et al.* (2011). The experimental setup is shown in figure 4. An elliptical-planform fin with an aspect ratio of 0.9 and a NACA0020 cross-section was fabricated using a flexible PVC polymer (MF Manufacturing). Here the aspect ratio is given

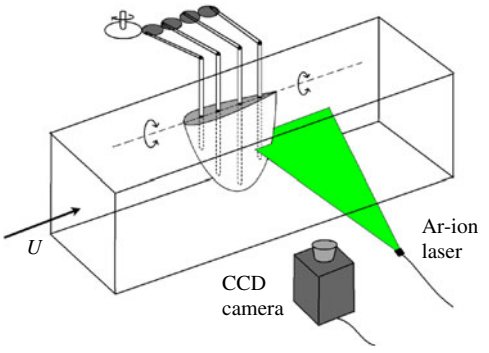

FIGURE 4. (Colour online) Experimental digital particle image velocimetry (DPIV) setup.

by b^2/S where b is the fin span length and S is the fin area. Four aluminium spars embedded into the fin are connected to a gear train that is driven by a DC motor (Pittman GM-9236S015-R1). A differential offset between subsequent gears allows the development of a chordwise travelling wave motion with wavelength λ, expressed in non-dimensional form as $\lambda^* = \lambda/L$, where L is the chord length at the root of the fin. Pivot points located at the root of the fin generate sinusoidal motion of the spars as the gear train is powered so that the amplitude of motion linearly increases along the span.

Experiments were conducted in a closed-loop water channel measuring 0.46 m wide, 0.3 m deep, and 2.44 m long. A free-stream flow velocity of $U = 0.06$ m s^{-1} was imposed corresponding to a chord-based Reynolds number of 11 600. Two-dimensional digital particle image velocimetry (DPIV) was conducted in the wake of the fin. The DPIV system used 93 μm hollow silver spheres (Potters Industries Inc. Conduct-O-Fil AGSL150 TRD) for flow seeding, a Spectra Physics 2020 continuous wave argon-ion laser light source, and a Redlake MotionXtra HG-LE 8 bit monochrome CCD camera. Software developed by Jiménez (2002) was used for the DPIV analysis, with tests by Chan *et al.* (2011) giving an estimated uncertainty of 1–5 % in the velocity measurements. The resolution of the camera and corresponding analysis yielded approximately 60 velocity vectors per chord length. The DPIV system was triggered using a timing-control system (Stanford Research Systems DG535) to acquire data for 20 consecutive oscillation periods. The data across all of these cycles are then averaged to yield time-averaged velocity fields.

The actual frequency of motion, not the nominal frequency, was experimentally measured and reported. There was no significant error in this measurement. A 512 CPR quadrature encoder was utilized to measure the period of motion. After gearing, this yielded a pulse train consisting of 6192 pulses per oscillation period. These data were typically sampled at 1 kHz, producing uncertainties of the order of 6–10 pulses per revolution, indicating that the period of motion was accurate to well within 1/100 s. For the lowest frequencies tested (0.3 Hz) the associated error in the apparatus frequency is $\pm 1 \times 10^{-3}$ Hz. Further details of the experiment and data analysis are given by Dewey *et al.* (2011).

5.1. *Measurement location*

The plane at the midspan of the fin was chosen to conduct the stability analysis. Since the amplitude of motion of the fin increases linearly with spanwise extent, this plane represents the average amplitude of motion for the fin. Also, Clark & Smits (2006)

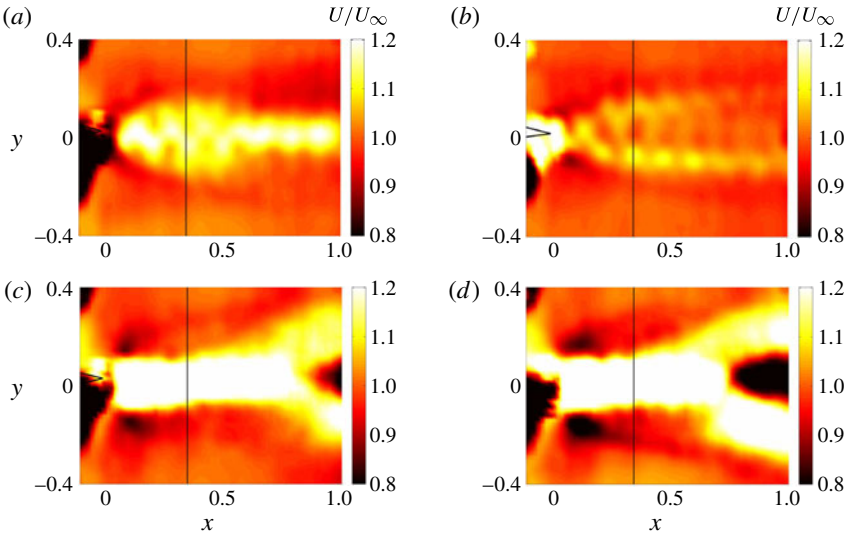

FIGURE 5. (Colour online) Time-averaged velocity fields for four different parameter sets: (*a*) $St = 0.2, \lambda^* = 4$; (*b*) $St = 0.2, \lambda^* = 2.4$; (*c*) $St = 0.3, \lambda^* = 4$; and (*d*) $St = 0.3, \lambda^* = 6$. The solid line is the velocity profile extraction location at 0.36 root chords downstream of the trailing edge of the midspan section. Refer to figure 1 for the definitions of the x and y axes. The x and y coordinates are non-dimensionalized with respect to the chord length, L.

and Dewey *et al.* (2011) noted that three-dimensional effects become more pronounced towards the tip of the fin where spanwise flows were observed. Spanwise flow would affect the direction of the maximally amplified perturbation waves such that they were no longer in the DPIV plane (Stuart 1987), and so we restrict our study to the nearly two-dimensional flow at the midspan of the fin.

The instantaneous velocity fields were time averaged and velocity profiles were extracted at a location 0.36 chord lengths downstream of the trailing edge. This downstream location was chosen as the nearest downstream location to the trailing edge where the length scale of the velocity jet changed slowly in the downstream direction, at least locally. This location was fixed for all of the cases in this paper. Figure 5 presents four of the examined time-averaged velocity fields. The solid line is the location at which the velocity profiles were extracted.

5.2. *Sensitivity analysis*

The sensitivity of the resonant frequencies to a change in downstream location was explored. Downstream stations in the range $0.36 < x < 0.44$ were analysed. This corresponds to the range nearest the trailing edge where the locally parallel flow assumption holds for the case of $\lambda^* = 4$. The velocity-profile resonant frequency variations were measured for $St = 0.2$ and $St = 0.3$. These two cases are found to be the closest to the wake resonant frequencies discussed later. An average variation in the wake resonant frequency of $St = \pm 0.03$ was found. The wake resonant frequency uncertainty is reflected in figures 11 and 13.

The sensitivity of resonant frequencies to uncertainty in the PIV measurements was also examined. An ideal velocity profile was analysed to find its resonant frequency:

$$U(y) = 1 + \mathrm{sech}^2(8y) \quad \text{for} \quad -1 \leqslant y \leqslant 1. \tag{5.1}$$

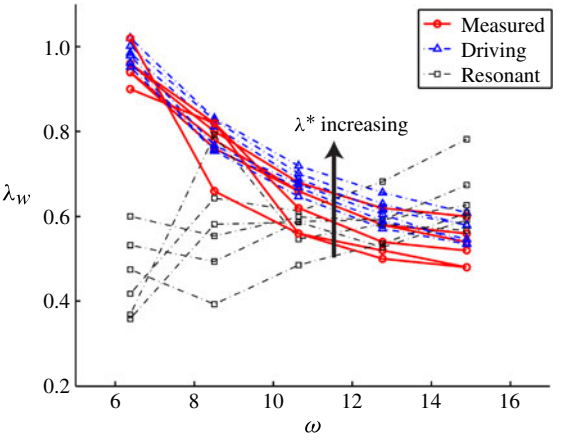

FIGURE 6. (Colour online) The experimentally measured vortex wavelength (open circle, solid line), perturbation wavelength at the driving frequency (open triangle, dashed line) and the perturbation wavelength at the velocity-profile resonant frequency (open circle, dashed line). The perturbation wavelength at the driving frequency closely matches the experimentally observed vortex wavelength.

The resonant frequency was calculated to be $\omega = 9.337$. Random noise was added to the ideal velocity profile with an amplitude equal to a percentage of the difference between the peak velocity and the free-stream velocity (up to 10 %). The analysis procedure previously described was then applied to the noisy velocity profile. A moving-average filter is included in this procedure to smooth out the second derivative of the velocity profile, $U''(y)$, which is necessary for the eigenvalue solution. At a noise amplitude of 10 % there was a 4 % variation in the resonant frequency.

6. Results

6.1. *Time-averaged velocity jet and the observed wake*

The formation of wavy jet structures is the hallmark of unsteady propulsion. The connection between the time-averaged velocity profiles and the observed wake structure will be established by first examining the vortex wavelength of the wake and then by inspecting the wake pattern ($2S$ or $2P$). Both the experimental observations and the linear stability calculations are shown to agree in both of these regards.

As discussed in § 4, stability curves display two important points: the driving and the resonant frequency of the profile. The most unstable eigenvalues at each frequency have been calculated for six different values of λ^* and five different Strouhal numbers for a total of 30 cases. The wavelengths of the wake perturbations are calculated from the real part of the eigenvalues as $\lambda_w = 2\pi/\alpha_r$. The observed vortex wavelength, λ_w, of the experiments is measured as the non-dimensional streamwise distance between vortices shed one period apart. Figure 6 shows that the wavelength calculated at the driving frequency matches the experiment closely, while the wavelength calculated at the resonant frequency does not. Therefore the eigenvalues and eigenmodes at the driving frequency are relevant to the physically observed wake structure, as expected.

To further motivate the use of time-averaged velocity profiles, the observed wake patterns may be compared to the eigenmodes at the driving frequency. As detailed examples, representative $2P$ and $2S$ wake structures will be examined from the

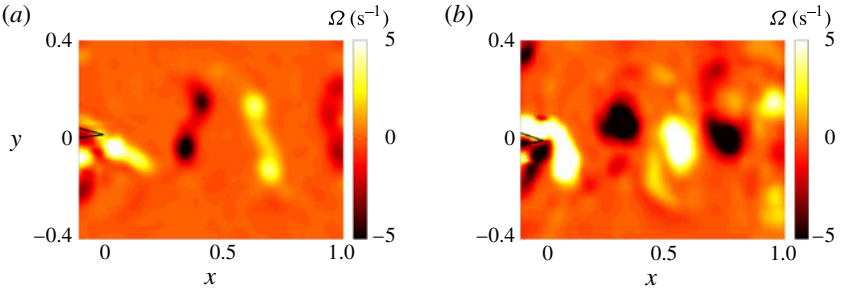

FIGURE 7. (Colour online) (*a*) 2*P* observed wake at $St = 0.2$, $\lambda^* = 2.4$; and (*b*) 2*S* observed wake at $St = 0.3$, $\lambda^* = 6$.

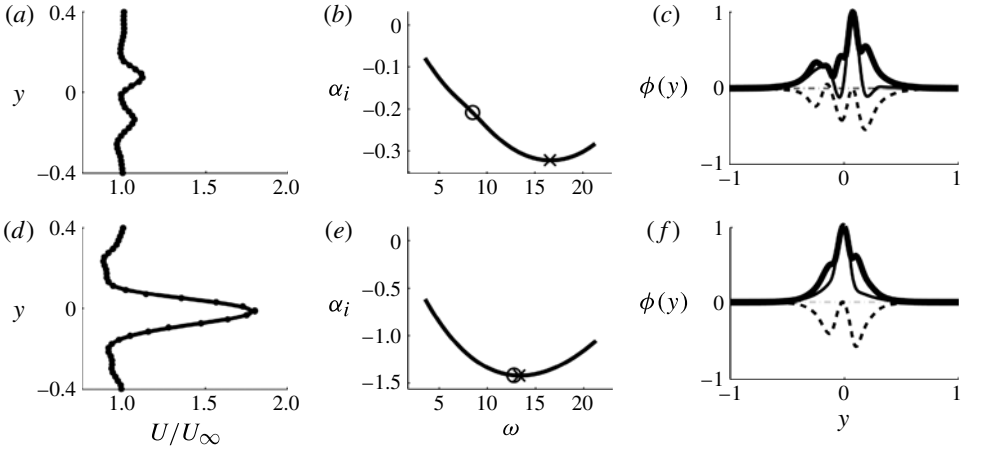

FIGURE 8. (*a*) 2*P* velocity profile at $St = 0.2$, $\lambda^* = 2.4$; (*b*) 2*P* stability curve; and (*c*) 2*P* eigenmode, $\phi(y)$. The real part of eigenmode is the thin solid line, the imaginary part is the thin dashed line and the modulus is the thick solid line. (*d*) 2*S* velocity profile at $St = 0.3$, $\lambda^* = 6$, (*e*) 2*S* stability curve and (*c*) 2*S* eigenmode, $\phi(y)$. The eigenmode convention used in (*f*) for the real part, imaginary part and modulus is the same as in (*c*).

experiment of Dewey *et al.* (2011). The clearest representation of each case can be seen in figure 7. Figures 7(*a*) and 7(*b*) show the experimentally observed vorticity patterns of the 2*P* and 2*S* wake structures for the parameters $St = 0.2$, $\lambda^* = 2.4$ and $St = 0.3$, $\lambda^* = 6$, respectively. Figures 5(*b*) and 5(*d*) show the corresponding time-averaged velocity fields of the 2*P* and 2*S* wakes, respectively.

The velocity profiles, associated stability curves and the associated eigenmodes are shown in figure 8. In the case of the 2*S* wake structure, the driving frequency and the resonant frequency of the velocity profile are seen to be nearly coincident, indicating that a peak in efficiency should occur at this parameter set (St, λ^*). This will be examined in more detail later in the paper. In the case of the 2*P* wake structure, the driving frequency does not coincide with the resonant frequency of the velocity profile, indicating that sub-optimal performance is expected at these operating parameters. Regardless of the optimality, the 2*P* wake structure shown in figure 7(*a*) is the clearest example of such a structure, due to the distance downstream that the structure persists

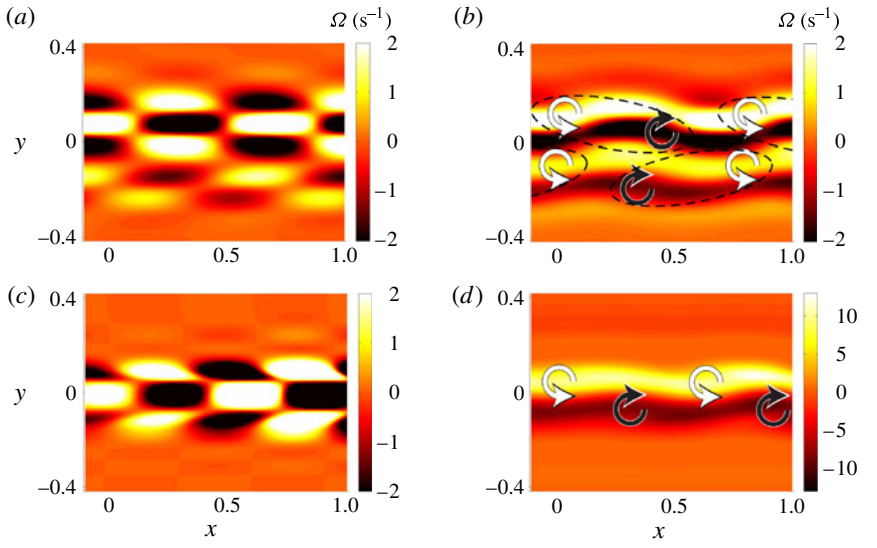

FIGURE 9. (Colour online) $2P$ wake (a) vorticity perturbations and (b) total vorticity. The vortex pairs of the $2P$ wake are marked with dashed ellipses. $2S$ wake (c) vorticity perturbations and (d) total vorticity. Vortex core locations are marked on the total vorticity plot where regions of vorticity are compressed together and oriented to lead to a single vortex core after nonlinear rollup.

and the near-equal circulation encapsulated in each of the vortex cores. In particular, the driving frequency is seen to be lower than the resonant frequency of the velocity profile. Presumably, if the driving frequency is increased then the fin could tune into the resonance of this mode for locally optimal efficiency. The eigenmodes, $\phi(y)$, are also shown for completeness.

Figure 9(a,c) shows the vorticity perturbations calculated at the driving frequency from the eigenmodes, $\phi(y)$, and the travelling wave, E, at a fixed time. The vorticity perturbations for the $2P$ and $2S$ modes are distinctly different, with five lobes of vorticity and three lobes of vorticity, respectively, at a fixed downstream location. The superposition of the base-flow vorticity and the perturbation vorticity, Ω_T, is given in figure 9(b,d). The total vorticity is the initial linear wake structure that will lead to the observed wake structure through nonlinear Biot–Savart-induced rollup. This can be seen clearly by examining the $2S$ initial linear wake in figure 9(d). The perturbations cause the base vorticity to undulate in the downstream direction and to compress and stretch regions of the vorticity. Regions of compression for the positive vorticity can be seen at locations approximately 0.1 and 0.7 chords downstream. Regions of compression for the negative vorticity can be observed at locations approximately 0.4 and 1 chords downstream. The regions of compression are paired with cross-stream displacements of the vorticity with the combined effect of vorticity to roll up and concentrate at these compression centres. This initial linear stage is akin to the linear waves seen in Kelvin–Helmholtz rollup (Helmholtz 1868; Kelvin 1871).

When the compression centres are marked with a vortex of the appropriate sign, the $2S$ initial linear wake clearly leads to the $2S$ wake structure as observed in figure 7(b). Figure 9(b) also has vortex centres marked even though the regions of compression are less pronounced. When the wake structure evolves through nonlinear rollup it is clear

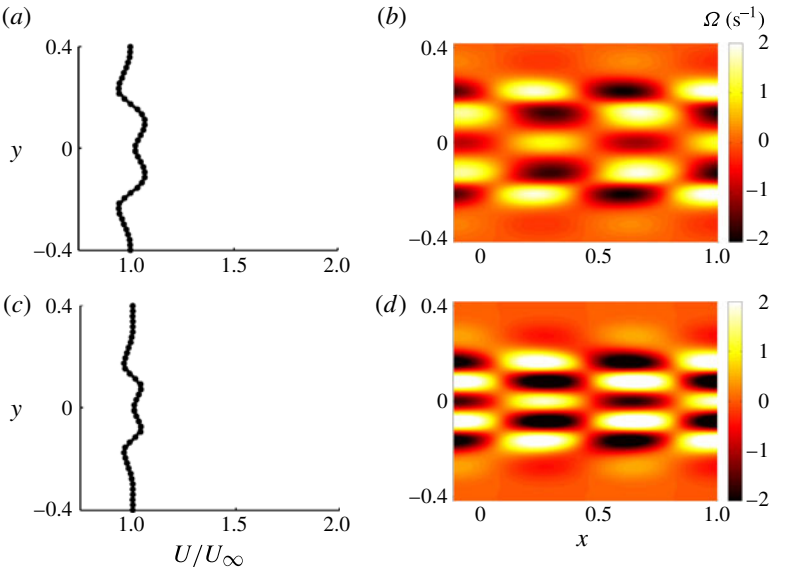

FIGURE 10. (Colour online) $2P$ velocity profile asymmetry is removed by (a) mirroring the negative-y data points about $y = 0$ and (c) mirroring the positive-y data points about $y = 0$. The subsequent vorticity perturbations for each case are shown in (b) and (d), respectively.

that a $2P$ structure will develop. The induced velocity between the nearest vortex cores of opposite sign produce a wavy jet pattern with a small component in the downstream direction signalling thrust production.

The vorticity perturbations in figure 9(a) display five lobes of vorticity at each downstream location, but two of the lobes are weaker than the other three. This asymmetry in the eigenmodes develops from the asymmetry of the velocity profile in figure 8(a). When the positive-coordinate data points of the velocity profile (figure 8a) are mirrored about $y = 0$ then figure 10(a) is obtained. Mirroring the negative data points about $y = 0$ will give figure 10(c). The vorticity perturbations for both cases are calculated and displayed in figure 10(b,d). When the profile is symmetric, the five lobes are symmetric about the origin and of nearly equivalent strength. The presence of five lobes of vorticity in the cross-stream direction will be regarded as the characteristic perturbation of a $2P$ wake structure.

We conclude that the time-averaged velocity fields retain much of the information about the measured flow field, in that both the observed wavelength and the wake pattern are recovered from a linear stability analysis of the time-averaged fields. We believe these results justify the use of linear stability analysis to help understand the physics of efficient unsteady propulsion.

6.2. *Resonant frequencies, wake transitions and efficient propulsion*

An important phenomenon observed by Clark & Smits (2006) was the existence of multiple peaks in propulsive efficiency with increasing Strouhal number. Later, Dewey *et al.* (2011) observed wake structure transitions from $2P$ to $2S$ as λ^* was increased at a fixed Strouhal number, or as Strouhal number was increased at a fixed λ^*. We are now in a position to connect these two observations, and to help explain the underlying physics.

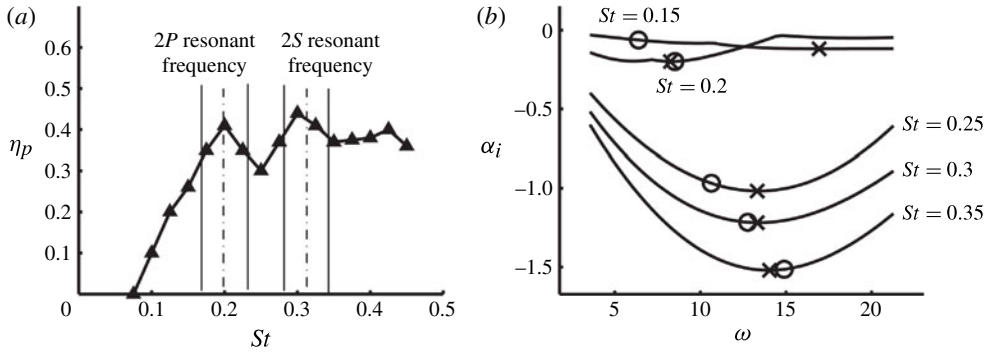

FIGURE 11. (*a*) Propulsive efficiency data of the elliptical fin measured by Clark & Smits (2006) for $\lambda^* = 4$. Dot-dashed lines denote the resonant frequencies found by the linear stability analysis. The solid lines denote the regions of uncertainty in the wake resonant frequencies. (*b*) Stability curves for five velocity profiles taken from DPIV data measured by Dewey *et al.* (2011). The **×** mark the resonant frequency of a stability curve while the **o** mark the driving frequency used to generate the velocity profile.

Figure 11(*a*) shows the efficiency data at $\lambda^* = 4$ measured by Clark & Smits (2006). Two peaks in efficiency can be observed at $St = 0.2$ and 0.3. The efficiency of a propulsor is an important performance metric; however, the thrust coefficient is also important. The thrust coefficient is defined as

$$C_T = \frac{\bar{T}}{\frac{1}{2}\rho S U_\infty^2}. \tag{6.1}$$

The propulsor planform area is S.

At the first efficiency peak $St = 0.2$, $C_T = 0.55$ and at the second efficiency peak $St = 0.3$, $C_T = 1.8$. Five velocity profiles were extracted from the DPIV data of Dewey *et al.* (2011) at five different frequencies corresponding to five St values evenly spaced between $0.15 \leqslant St \leqslant 0.35$. The corresponding stability curves are shown in figure 11(*b*). The jet resonant frequencies are plotted (**×**) as well as the jet driving frequencies (**o**).

In the cases where the driving frequency is nearly coincident with the jet resonant frequency, a peak in efficiency is expected. At $St = 0.2$ the driving frequency is nearly coincident with the resonant frequency and the two frequencies are also nearly coincident at $St = 0.3$. In figure 11(*a*), two dot-dashed lines have been plotted that show these two cases and they are labelled as the wake resonant frequencies. The two wake resonant frequencies from the linear stability analysis match closely to the two observed peaks in efficiency. This confirms the previously measured efficiency data as well as offering two insights: (i) when the driving frequency of the fin matches a wake resonant frequency a peak in efficiency occurs; and (ii) when multiple peaks in efficiency occur there are multiple wake resonant frequencies.

The vorticity eigenmode at the first peak in efficiency ($St = 0.2$) is presented in figure 12(*b*). This vorticity perturbation matches the characteristic $2P$ vorticity perturbation with some asymmetry. There are three weak lobes of vorticity in the negative-y range and three strong lobes of vorticity in the positive-y range. The two lobes of vorticity closest to the y origin have the same sign and therefore can be considered as a single lobe, giving the five characteristic lobes of vorticity seen in

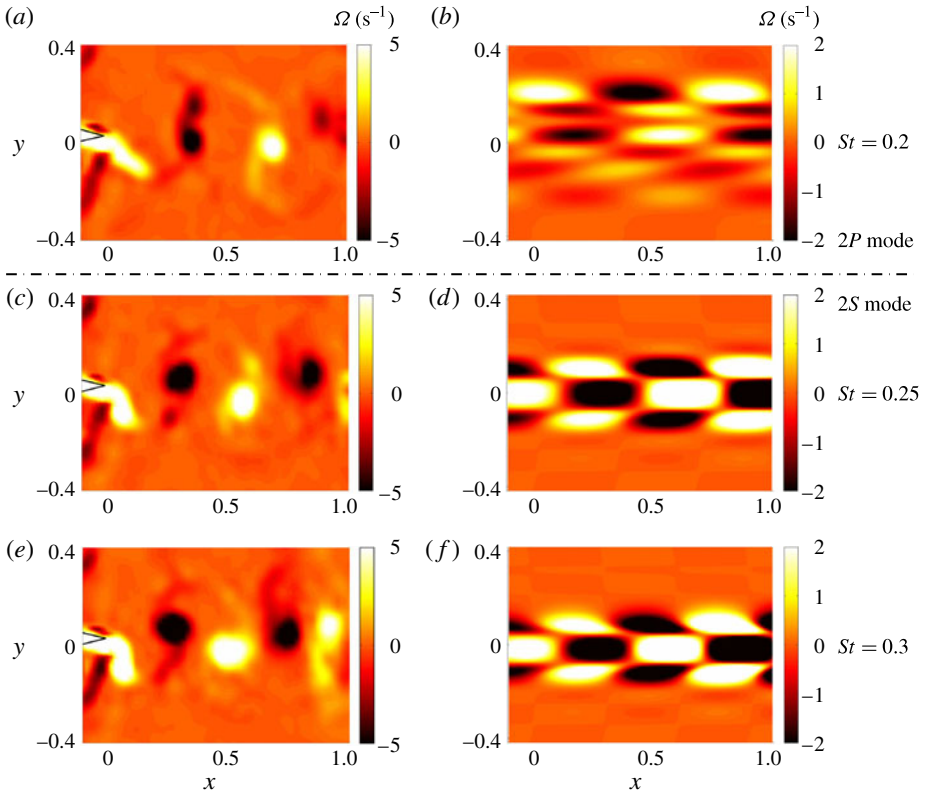

FIGURE 12. (Colour online) Observed wake structures for $\lambda^* = 4$ at: (*a*) $St = 0.2$; (*c*) $St = 0.25$ and (*e*) $St = 0.3$. The respective vorticity perturbations are shown in (*b*), (*d*) and (*f*). A transition from a 2*P* wake to a 2*S* wake (dot-dashed line) is observed.

the 2*P* perturbations. Indeed, the observed wake structure displays a 2*P* wake structure in the near wake ($x < 0.5$). In fact, this wake structure displays a bimodal behaviour within the field of measurement. Figure 5(*a*) shows the time-averaged velocity field. Near $x = 0.5$ a transition from 2*P* to 2*S* is occurring, which is reflected in the time-averaged velocity field. Figure 6 of Dewey *et al.* (2011) highlights the case where $\lambda^* = 4$, $St = 0.2$ to be the first instance where a 2*P* structure emerges in the near wake as λ^* is decreased from $\lambda^* = \infty$ with $St = 0.2$.

The wake structures and vorticity eigenmodes for $St = 0.25$ and 0.3 shown in figure 12(*c–f*) display the characteristics of a 2*S* wake structure. Each of the wake resonant frequencies can now be associated with a specific wake mode. There is a resonant frequency for the 2*P* wake mode and a resonant frequency for the 2*S* wake mode (labelled in figure 11*a*).

We now examine the efficiency data at $\lambda^* = 6$ measured by Clark & Smits (2006), as shown in figure 13(*a*). At the estimated efficiency peak $St = 0.175$, $C_T = 0.3$ and at the second efficiency peak $St = 0.3$, $C_T = 2$. The stability curves calculated for the range $0.15 \leqslant St \leqslant 0.35$ are displayed in figure 13(*b*). One fin resonant frequency is found near $St = 0.3$. By examining the vorticity eigenmodes at $St = 0.3$ (figure 14), this resonant frequency is associated with a 2*S* wake mode. In terms of efficiency,

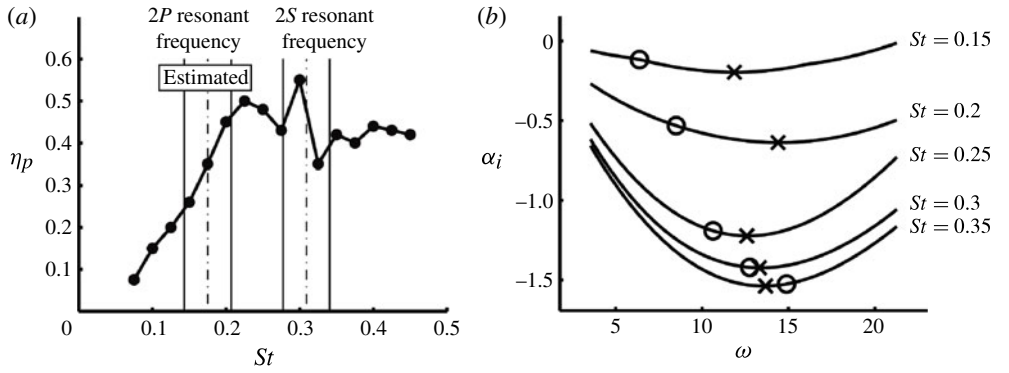

FIGURE 13. (*a*) Propulsive efficiency data of the elliptical fin measured by Clark & Smits (2006) for $\lambda^* = 6$. Dot-dashed lines denote the resonant frequencies found by the linear stability analysis. The solid lines denote the regions of uncertainty in the wake resonant frequencies. (*b*) Stability curves for five velocity profiles taken from DPIV data measured by Dewey *et al.* (2011). The **×** mark the resonant frequency of a stability curve while the **o** mark the driving frequency used to generate the velocity profile.

there is excellent agreement at this Strouhal number, where the efficiency peak nearly matches the wake resonant frequency calculated from the linear analysis.

The stability curves in figure 13(*b*) also admit an oddity. The case of $St = 0.15$ shows the driving frequency at a lower frequency than the velocity profile resonant frequency. Tuning the driving frequency higher should decrease the separation distance between the driving and resonant frequencies, but instead the separation increases while the driving frequency remains at a value lower than the resonant frequency. This result suggests that a wake resonant frequency was passed between $St = 0.15$ and $St = 0.2$. Additional PIV data within this St range (not available in Dewey *et al.* 2011) would be necessary to confirm this suggestion. On this basis an estimated $2P$ wake resonant frequency has been added to the efficiency curve in figure 13(*a*), in the range $0.15 < St < 0.2$.

By examining the vorticity eigenmodes in figure 14, additional insight can be obtained. The eigenmode at $St = 0.15$ is the characteristic $2P$ mode while at $St = 0.2$ it is the characteristic $2S$ mode. It is clear that this signals a wake transition in the range $0.15 < St < 0.2$, as reflected in the observed wake structures. The wake mode transition further supports the conclusion that a $2P$ wake resonant frequency may have been passed.

At first glance, the estimated resonant frequency does not appear to agree very well with the experimentally measured peak in efficiency at $St = 0.225$. However, Buchholz, Clark & Smits (2008) report the uncertainty in the experimental efficiency measurements to be $\pm 20\,\%$ at $St = 0.2$ and 0.225, so this may reflect the experimental uncertainty in establishing the location of the actual peak.

6.3. *Wake resonance theory*

From the previous results, a theoretical framework is suggested to help explain the physics of efficient unsteady propulsion. First, tuning the driving frequency to a wake resonant frequency results in a local peak in efficiency. Second, there may be multiple wake resonant frequencies relating to multiple peaks in efficiency. Third, some observed wake structures will transition when the wake instability modes transition.

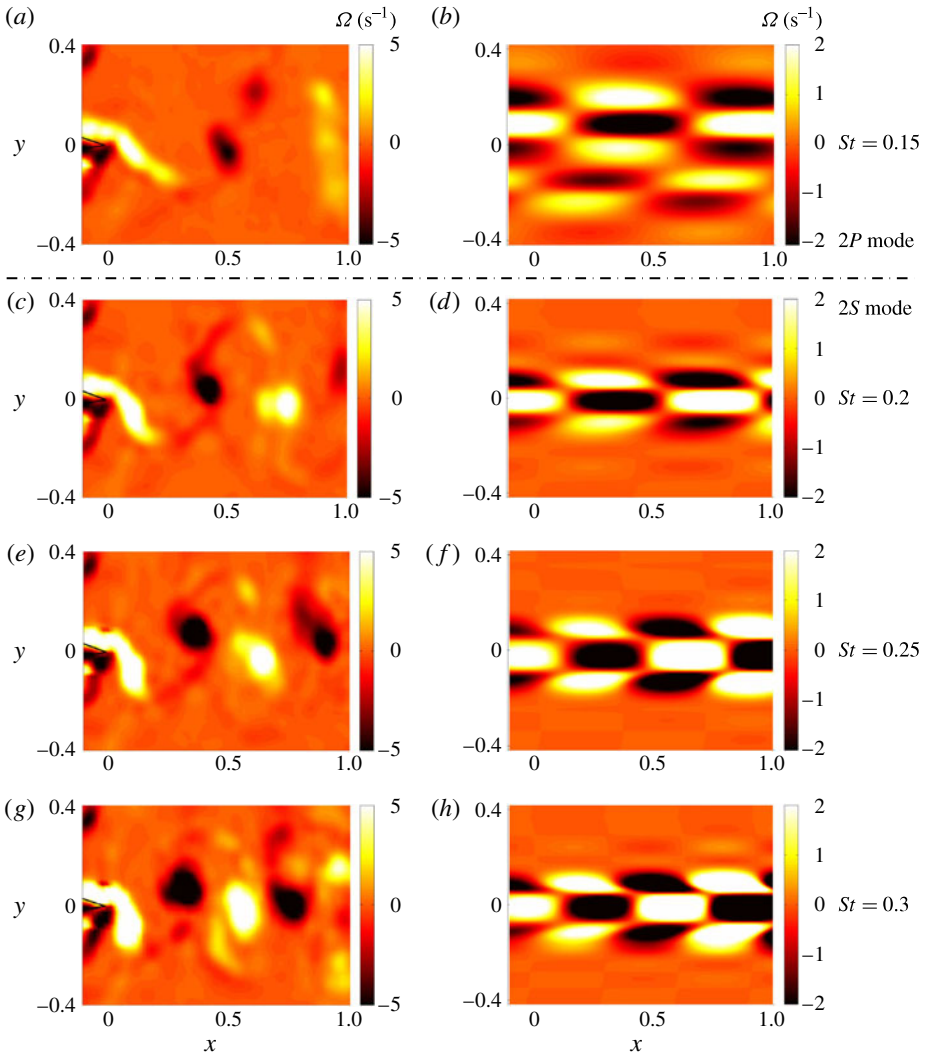

FIGURE 14. (Colour online) Observed wake structures for $\lambda^* = 6$ at: (*a*) $St = 0.15$; (*c*) $St = 0.2$; (*e*) $St = 0.25$; and (g) $St = 0.3$. The respective vorticity perturbations are shown in (*b*), (*d*), (*f*) and (*h*). A transition from a 2*P* wake to a 2*S* wake (dot-dashed line) is observed.

It can no longer be claimed that a 2*S* wake structure is the only wake mode that leads to efficient locomotion because other wake modes such as a 2*P* mode can also lead to locally efficient propulsion. The global maximum in efficiency, at this point, cannot be attributed to a particular wake mode. It is hypothesized that the globally most efficient wake mode to utilize will be based on the kinematics of motion as well as the shape of the fin or device. That is, for one set of kinematics and one propulsor shape a 2*P* mode may be the most efficient wake mode to utilize, while for another set of kinematics and another propulsor shape a 2*S* mode may be the optimally efficient wake mode.

As a direct extension of the theory, other more elaborate wake modes (Lewin & Haj-Hariri 2003; Lentink *et al.* 2008) are also expected to have their own wake

resonant frequencies, although this has not been shown here. Caution must be used in applying the spatial stability analysis to wakes with non-parallel flow, though, such as the bifurcating wake in Dewey *et al.* (2011). Wakes that are locally non-parallel would need to be analysed using a global stability analysis (Chomaz 2005).

7. Conclusions

Flapping fins shed a series of vortices in their wakes that produce a wavy jet structure. In analogy to bluff-body wake analysis, the time-averaged jet structure can be analysed for its most unstable frequency, described here as the hydrodynamic resonant frequency of the velocity profile. When the driving frequency of the fin is tuned to the resonant frequency of the velocity profile it is shown that a peak in propulsive efficiency occurs at the wake resonant frequency. Moreover, there can be multiple wake resonant frequencies and thus multiple peaks in efficiency as the driving frequency is varied. Linear spatial stability analysis is utilized to also calculate the linear vorticity perturbations at each driving frequency. It is shown that these modes capture both the wavelength of the shed vortices and also the wake pattern found in the experiment, motivating the analysis of the time-averaged jet flow. Furthermore, different resonant frequencies were found to also correspond to different resonant modes. When the wake instability mode transitioned it was found that the observed wake structure also transitioned. In this study wake patterns beyond the reverse von Kármán vortex street were considered. Both $2P$ and $2S$ wake modes were found to be efficient modes of propulsion. Remarkable agreement with experimental data is obtained by utilizing a one-dimensional analysis to study a three-dimensional wake structure, thus showing the robustness and broad applicability of the technique.

Acknowledgement

The authors would like to acknowledge funding from the Office of Naval Research through the MURI program on Biologically-Inspired Autonomous Sea Vehicles (Program Manager: Dr R. Brizzolara, Contract No. N00014-08-1-0642).

REFERENCES

ANDERSON, J. M., STREITLIEN, K., BARRETT, D. S. & TRIANTAFYLLOU, M. S. 1998 Oscillating foils of high propulsive efficiency. *J. Fluid Mech.* **360**, 41–72.

BRIDGES, T. J. & MORRIS, P. J. 1984*a* Differential eigenvalue problems in which the parameter appears nonlinearly. *J. Comput. Phys.* **55** (3), 437–460.

BRIDGES, T. J. & MORRIS, P. J. 1984b Spectral calculations of the spatial stability of non-parallel boundary layers, *AIAA Paper* 84-0437, *AIAA 22nd Aerospace Sciences Meeting*.

BUCHHOLZ, J. H. J., CLARK, R. P. & SMITS, A. J. 2008 Thrust performance of unsteady propulsors using a novel measurement system, and corresponding wake patterns. *Exp. Fluids* **45** (3), 461–472.

BUCHHOLZ, J. H. J. & SMITS, A. J. 2008 The wake structure and thrust performance of a rigid low-aspect-ratio pitching panel. *J. Fluid Mech.* **603**, 331–366.

CHAN, A. S., DEWEY, P. A., JAMESON, A., LIANG, C. & SMITS, A. J. 2011 Vortex suppression and drag reduction in the wake of counter rotating cylinders. *J. Fluid Mech.* **679**, 343–382.

CHOMAZ, J. M. 2005 Global instabilities in spatially developing flows: non-normality and nonlinearity. *Annu. Rev. Fluid Mech.* **37**, 357–392.

CLARK, R. P. & SMITS, A. J. 2006 Thrust production and wake structure of a batoid-inspired oscillating fin. *J. Fluid Mech.* **562**, 415–429.

DEWEY, P. A., CARRIOU, A. & SMITS, A. J. 2012 On the relationship between efficiency and wake structure of a batoid-inspired oscillating fin. *J. Fluid Mech.* **691**, 245–266.

GANTMACHER, F. R. 1959 *The Theory of Matrices*, vol. 1. Chelsea.

GASTER, M. 1965 On the generation of spatially growing waves in a boundary layer. *J. Fluid Mech.* **22**, 433–441.

GROSCH, C. E. & SALWEN, H. 1978 The continuous spectrum of the Orr–Sommerfeld equation. Part 1. The spectrum and the eigenfunctions. *J. Fluid Mech.* **87** (1), 33–54.

HAJ-HARIRI, H. 1988 Transformations reducing the order of the parameter in differential eigenvalue problems. *J. Comput. Phys.* **77** (2), 472–484.

HELMHOLTZ, H. 1868 On discontinuous movements of fluids. *Phil. Mag* **36** (4), 337–346.

HULTMARK, M., LEFTWICH, M. & SMITS, A. J. 2007 Flowfield measurements in the wake of a robotic lamprey. *Exp. Fluids* **43** (5), 683–690.

HUERRE, P. & MONKEWITZ, P. A. 1985 Absolute and convective instabilities in free shear layers. *J. Fluid Mech.* **159**, 151–168.

JIMÉNEZ, J. M. 2002 Low Reynolds number studies in the wake of a submarine model using particle image velocimetry. Master's thesis, Princeton University, Princeton, NJ, USA.

VON KÁRMÁN, T. & BURGERS, J. M. 1935 General aerodynamic theory-perfect fluids. In *Aerodynamic Theory II*, (ed. W. F. Durand), pp. 280–310. Dover Publications, 1963.

KARNIADAKIS, G. & TRIANTAFYLLOU, G. 1989 Frequency selection and asymptotic states in laminar wakes. *J. Fluid Mech.* **199**, 441–469.

KELVIN W. T., LORD 1871 Hydrokinetic solutions and observations. *Phil. Mag.* **42**, 362–377.

KOOCHESFAHANI, M. M. 1989 Vortical patterns in the wake of an oscillating airfoil. *AIAA J.* **27**, 1200–1205.

LAUDER, G. V. & DRUCKER, E. G. 2002 Forces, fishes, and fluids: hydrodynamic mechanisms of aquatic locomotion. *Physiology* **17** (6), 235–240.

LENTINK, D., MUIJRES, F. T., DONKER-DUYVIS, F. J. & VAN LEEUWEN, J. L. 2008 Vortex-wake interactions of a flapping foil that models animal swimming and flight. *J. Expl Biol.* **211** (2), 267–273.

LEWIN, G. C. & HAJ-HARIRI, H. 2003 Modelling thrust generation of a two-dimensional heaving aerofoil in a viscous flow. *J. Fluid Mech.* **492**, 339–362.

MACK, L. M. 1976 A numerical study of the temporal eigenvalue spectrum of the Blasius boundary layer. *J. Fluid Mech.* **73** (3), 497–520.

MATTINGLY, G. E. & CRIMINALE, W. O. 1972 The stability of an incompressible two-dimensional wake. *J. Fluid Mech.* **51** (2), 233–272.

ORSZAG, S. A. 1971 Accurate solution of the Orr–Sommerfeld stability equation. *J. Fluid Mech.* **50** (4), 689–703.

SALWEN, H. & GROSCH, C. E. 1981 The continuous spectrum of the Orr–Sommerfeld equation. Part 2. Eigenfunction expansions. *J. Fluid Mech.* **104**, 445–465.

STUART, J. T. 1987 Instability, three-dimensional effects, and transition in shear flows. In *Perspectives in Turbulence Studies* (ed. H. U. Meier & P. Bradshaw). pp. 1–25. Springer.

TAYLOR, G. K., NUDDS, R. L. & THOMAS, A. L. R. 2003 Flying and swimming animals cruise at a Strouhal number tuned for high power efficiency. *Nature* **425** (6959), 707–711.

TRIANTAFYLLOU, G. S., TRIANTAFYLLOU, M. S. & CHRYSSOSTOMIDIS, C. 1986 On the formation of vortex streets behind stationary cylinders. *J. Fluid Mech.* **170**, 461–477.

TRIANTAFYLLOU, G. S., TRIANTAFYLLOU, M. S. & GROSENBAUGH, M. A. 1993 Optimal thrust development in oscillating foils with application to fish propulsion. *J. Fluids Struct.* **7** (2), 205–224.

TRIANTAFYLLOU, M. S., TRIANTAFYLLOU, G. S. & GOPALKRISHNAN, R. 1991 Wake mechanics for thrust generation in oscillating foils. *Phys. Fluids* A **3**, 2835.

TYTELL, E. D., BORAZJANI, I., SOTIROPOULOS, F., BAKER, T. V., ANDERSON, E. J. & LAUDER, G. V. 2010 Disentangling the functional roles of morphology and motion in the swimming of fish. *Integr. Compar. Biol.* **50** (6), 1140.

WILLIAMSON, C. H. K. & ROSHKO, A. 1988 Vortex formation in the wake of an oscillating cylinder. *J. Fluids Struct.* **2** (4), 355–381.